The Effect of a Nonuniform Planetary Albedo on the Interpretation of Earth Radiation Budget Observations

MICHAEL D. KING AND ROBERT J. CURRAN

Laboratory for Atmospheric Sciences, Goddard Space Flight Center, NASA, Greenbelt, MD 20771

(Manuscript received 6 August 1979, in final form 22 January 1980)

ABSTRACT

The flux density measured at satellite altitude with a fixed field of view radiometer differs from the true flux density reflected by the earth-atmosphere system within the field of view of the radiometer. This difference is due to angular response characteristics of the radiometer, solid angle effects due to geometry, and angular reflectance effects of the earth-atmosphere system. All of these effects lead to uncertainties in the interpretation of instantaneous earth radiation budget measurements. The differences between the true flux density and the measured flux density are shown to be significant when the field of view of the radiometer is large and when the atmosphere has a nonuniform, or spatially dependent, reflectance (albedo). A simulation experiment is described whereby the scene within the field of view of a nadir looking sensor is divided into a large number of equal area elements, each of which reflects radiation with one of two different reflectance models (corresponding to cloud-free and cloudy areas). The conditional mean values of the measured flux density, given values of the true flux density, are shown to differ significantly from the conditional means of the inverse problem, that of finding the mean value of the true flux density given a value for the measured flux density. The differences between the true flux density and the measured flux density are examined as a function of satellite altitude, field of view of the radiometer and solar zenith angle (including the effects of a terminator within the field of view) for both Lambertian and non-Lambertian reflectance models.

1. Introduction

Spatial imbalances between absorbed solar radiation and emitted thermal radiation are known to be a primary cause of energy transport by the atmosphere and ocean. Observations of the components of the earth's radiation budget have been made since the earliest earth orbiting satellites. These early satellite observations have primarily been used in phenomenological descriptions of the geographical and seasonal variation of the longwave and shortwave flux densities [see, e.g., Vonder Haar and Suomi (1971) or Raschke *et al.* (1973)]. More recent satellite data have been used in quantitative applications by Oort and Vonder Haar (1976) and by Ellis *et al.* (1978) where the correlation between the radiation components and other parameters describing the earth's climate was tested. Earth radiation budget data have been used in parameterization studies of the earth's climate based on energy balance climate models by Lian and Cess (1977), Coakley (1979) and North and Coakley (1979), among others. As these data are used in more sophisticated climate applications the need increases for realistic estimates of the errors associated with these data.

The present effort is an attempt to understand and bound the errors associated with the transformation of satellite-measured shortwave flux densities into radiation flux densities leaving the top of the atmosphere. Jacobowitz *et al.* (1979), in analyzing the Nimbus 6 Earth Radiation Budget (ERB) data, have considered the various sources of instrumental error. As a result of their analysis of instrumental errors it was possible to establish the globally averaged annual radiation balance of the earth-atmosphere system to a high degree of accuracy. Globally averaged data collected from satellite-borne, flat plate radiometers do not require the transformation of satellite measurements to top of the atmosphere flux densities. However, geographical descriptions of the radiation parameters do require this transformation. Quantitative use of these data on a regional basis necessitates an analysis of the errors involved in this transformation process.

The shortwave or solar component of the radiation budget has been selected for the present investigation because of the lack of existing error analyses in this spectral region. The sun, as an external source of finite angular extent, can produce a strongly anisotropic and azimuthally dependent reflected radiation field for large solar zenith angles. The emitted longwave radiation, on the other hand, is azimuthally independent when the sources are imbedded within a horizontally stratified atmosphere. Because of the particular problems involved in describing the complete angular properties of the

shortwave reflected intensities, the error analysis presented here considers only the shortwave spectral region. The same techniques can, of course, be applied to the emitted longwave radiation case.

In the present study the differences between the flux density measured at satellite altitude and the true reflected flux density within the field of view of a nadir looking satellite sensor are investigated. The differences between the true flux density and the measured flux density are examined as a function of satellite altitude and field of view for the case of a nonuniform, or spatially dependent, reflected flux density (or albedo). This is analogous to the situation in which portions of the field of view are filled with high-albedo clouds while the remaining portions are cloud free and have much lower albedos. The effect of scene inhomogeneity is first investigated by using the random positioning of isotropically reflecting elements of differing albedos within the field of view. Finally, the compounded effects of scene inhomogeneity and the angular distribution of the reflected radiation field are investigated using realistic cloudy and cloud-free angular dependencies.

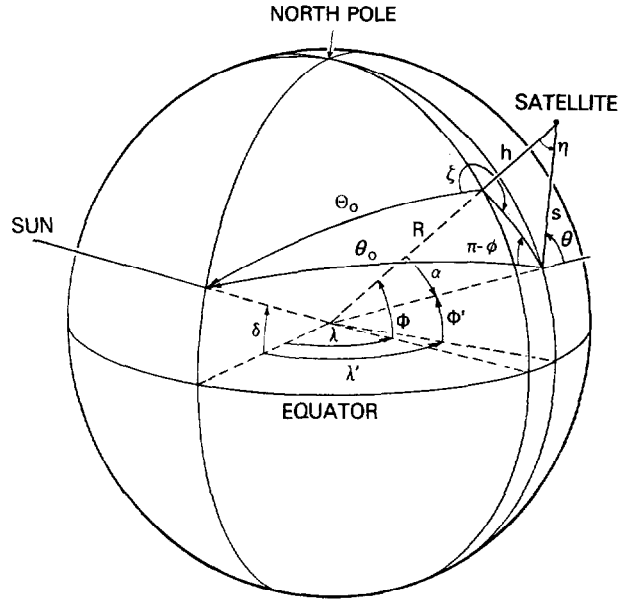

FIG. 1. Schematic illustration of the earth-atmosphere system illuminated by the sun at solar declination angle δ and viewed by a satellite at height h above the atmosphere. The angles and distances defined in this figure are discussed in the text.

2. Formulation of the problem

The shortwave component of the earth radiation budget arises from incoming solar radiation which is reflected by the earth-atmosphere system. From measurements of the reflected radiation at satellite altitude it is desirable to determine corresponding values of the reflected flux density at the top of the radiatively active layers of the atmosphere, defined as the altitude above which the radiation field suffers negligible attenuation. Both the incident flux density as well as the reflected flux density are functions of location on the globe. If a satellite is located at a latitude Φ and a local hour angle λ, as illustrated in Fig. 1, the solar zenith angle at the subsatellite point is given by Θ_0. In this figure the earth-atmosphere system is approximated by a sphere of radius R and the satellite is positioned at a height h above the surface of the sphere. If one assumes that the top of the radiatively active layers of the atmosphere is at a height of 30 km above the earth's surface, the height H of the satellite is given by $H = h + 30$ km. It is convenient, for purposes of the present discussion, to define the location of an element of area on the surface of the sphere at a latitude Φ' and a local hour angle λ' in terms of an earth central angle α and an azimuth angle ζ (see Fig. 1). These coordinates are based on the location of an element on the surface of the sphere with respect to the plane containing the sun, the center of the earth and the satellite. In terms of these coordinates and the solar zenith angle at the subsatellite point Θ_0, the cosine of the solar zenith angle ($\cos\theta_0$) at any particular location on the globe can be written as

$$\cos\theta_0 = \cos\Theta_0 \cos\alpha + \sin\Theta_0 \sin\alpha \cos\zeta. \quad (1)$$

The reflected flux density $F^+(\alpha, \zeta; \theta_0)$ at any point (α,ζ) on the surface of the sphere can be expressed as an integral of the reflected intensity $I(\alpha, \zeta; \theta_0, \theta, \phi)$ and is given by

$$F^+(\alpha, \zeta; \theta_0) = \int_0^{2\pi} \int_0^{\pi/2} I(\alpha, \zeta; \theta_0, \theta, \phi) \cos\theta \sin\theta \, d\theta d\phi, \quad (2)$$

where θ is the angle between the direction of propagation and the local vertical and ϕ the azimuth angle between the direction of propagation of the reflected radiation and the incident solar direction. The angles θ and $\pi - \phi$ are illustrated in Fig. 1 for radiation propagating in the particular direction of the satellite. The plane albedo $a(\alpha, \zeta; \theta_0)$ of the earth-atmosphere system can be defined in terms of the reflected flux density by

$$F^+(\alpha, \zeta; \theta_0) = \begin{cases} F_0 a(\alpha, \zeta; \theta_0) \cos\theta_0, & \theta_0 < 90° \\ 0, & \theta_0 \geq 90°, \end{cases} \quad (3)$$

where F_0 is the solar flux density incident on the top of the atmosphere.

At any particular instant of time a satellite sensor is only capable of estimating the mean flux density within the instantaneous field of view of the sensor. For the case of a nadir looking radiometer with a circular field of view, the mean reflected flux density (F_{true}) within the field of view of the radiometer is given by

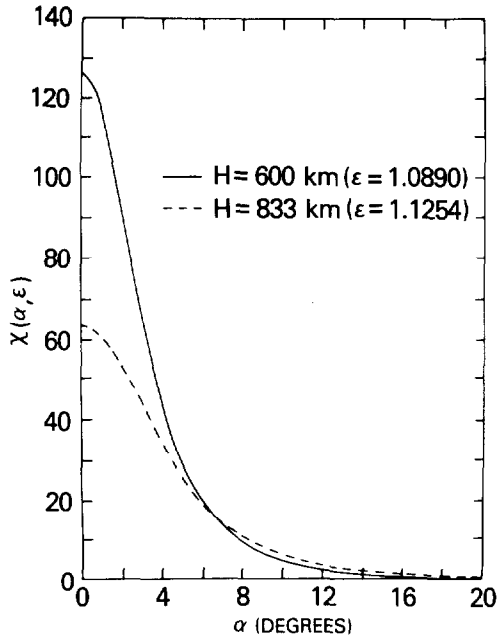

FIG. 2. Variation of $\chi(\alpha,\epsilon)$ as a function of α for satellites at two different altitudes above the surface of the earth. When H = 600 (833) km the corresponding value of ϵ = 1.0890 (1.1254).

$$F_{\text{true}} = \frac{\int_0^{2\pi}\int_0^{\alpha_m} F^+(\alpha,\zeta;\theta_0)R^2 \sin\alpha\, d\alpha d\zeta}{\int_0^{2\pi}\int_0^{\alpha_m} R^2 \sin\alpha\, d\alpha d\zeta}$$

$$= \frac{1}{2\pi(1-\cos\alpha_m)}\int_0^{2\pi}\int_0^{\alpha_m} F^+(\alpha,\zeta;\theta_0) \times \sin\alpha\, d\alpha d\zeta, \quad (4)$$

where α_m is the earth central angle measured from the satellite position to the edge of the instrument's instantaneous field of view.

Since global radiation budget measurements can only be made at viable satellite altitudes (*viz.*, $H \gtrsim 500$ km for stable orbits), the measured flux density at satellite altitude differs from the true flux density at the top of the atmosphere, given by (4). For a nadir looking satellite sensor which integrates the reflected intensity field with an angular response function of $\cos\eta$, where η is the angle at the satellite between the satellite nadir direction and the direction of an element of area on the surface of the sphere (see Fig. 1), the measured flux density is given by

$$F_{\text{meas}} = \int_{\text{IFOV}} I(\alpha,\zeta;\theta_0,\theta,\phi)\cos\eta\, d\omega. \quad (5)$$

In the earliest earth orbiting satellites, for which satellite stabilization was a difficult task, omnidirectional sensors were used to infer the earth radiation budget components. Since these early satellites (such as Explorer VII) did not contain sensors with $\cos\eta$ response functions, much interest revolved around converting these measurements to the vertical flux components at the satellite (see, e.g., Bignell, 1961). In Eq. (5) the integration is over the instantaneous field of view (IFOV) of the satellite sensor and $d\omega$ is the solid angle subtended at the satellite by an element of area $dA = R^2 \sin\alpha\, d\alpha d\zeta$ on the surface of the sphere. If one defines s as the distance from the satellite to an elemental area, as illustrated in Fig. 1, it immediately follows that

$$F_{\text{meas}} = R^2 s^{-2}\int_0^{2\pi}\int_0^{\alpha_m} I(\alpha,\zeta;\theta_0,\theta,\phi) \times \cos\eta\cos\theta\sin\alpha\, d\alpha d\zeta. \quad (6)$$

Applying the law of cosines to the geometry illustrated in Fig. 1, the measured flux density can be shown to yield

$$F_{\text{meas}} = \int_0^{2\pi}\int_0^{\alpha_m} I(\alpha,\zeta;\theta_0,\theta,\phi) \times \frac{(\epsilon-\cos\alpha)(\epsilon\cos\alpha-1)}{(1+\epsilon^2-2\epsilon\cos\alpha)^2}\sin\alpha\, d\alpha d\zeta, \quad (7)$$

where

$$\epsilon = \frac{R+h}{R}. \quad (8)$$

The factor

$$\chi(\alpha,\epsilon) = \frac{(\epsilon-\cos\alpha)(\epsilon\cos\alpha-1)}{(1+\epsilon^2-2\epsilon\cos\alpha)^2} \quad (9)$$

which appears in Eq. (7) is azimuthally independent and acts to weight the reflected intensity field incident on the satellite sensor such that equal-area reflecting elements of the earth-atmosphere system having equal intensities contribute differently depending on their location within the instrument's field of view.

Fig. 2 illustrates $\chi(\alpha,\epsilon)$ as a function of α for satellites located at two different heights, H = 600 km and H = 833 km. These correspond to anticipated altitudes of two members of a three satellite Earth Radiation Budget Experiment (ERBE). It is clear from this figure that contributions to the measured flux density from elements of the atmosphere near the subsatellite point (small values of α) are greater than contributions from similarly reflecting elements located near the edge of the instrument's field of view (large values of α). Satellites at both altitudes will contain two shortwave fixed field of view radiometers, a medium field of view (MFOV) radiometer defined such that

$$\alpha_m = 5.0°, \quad (10)$$

and a wide field of view (WFOV) radiometer defined such that the instrument views the entire earth-atmosphere system, horizon to horizon. From the geometric definitions given above, it can readily be shown that this is equivalent to a maximum earth central angle α_m given by

$$\alpha_m = \cos^{-1}(1/\epsilon). \tag{11}$$

For the two altitudes illustrated in Fig. 2, $\alpha_m = 23.33$ and 27.31° for $H = 600$ and 833 km, respectively.

Although the measured flux density necessarily consists of radiation incident from all directions within the radiometer's instantaneous field of view (i.e., $0 \leq \alpha \leq \alpha_m$), the majority of the signal arises from radiation incident from small values of α (cf. Fig. 2). As a consequence, it would be possible to relate F_{meas} to a true flux density defined as a mean flux density over an area smaller than the entire field of view. The results presented below (Section 4) assume the integration limits to be $0 \leq \alpha \leq \alpha_m$ for both F_{meas} and F_{true}. The comparison between F_{meas} and an alternative definition of F_{true} could be evaluated using the same techniques outlined below.

The similarities and differences between the true flux density F_{true} and the measured flux density F_{meas} are made clearer if we define a bidirectional reflectance function $\rho(\alpha, \zeta; \theta_0, \theta, \phi)$ such that

$$I(\alpha, \zeta; \theta_0, \theta, \phi) = \pi^{-1}F^+(\alpha, \zeta; \theta_0)\rho(\alpha, \zeta; \theta_0, \theta, \phi). \tag{12}$$

Substituting (12) back into (2), the bidirectional reflectance function is seen to satisfy the normalization condition

$$1 = \pi^{-1}\int_0^{2\pi}\int_0^{\pi/2} \rho(\alpha, \zeta; \theta_0, \theta, \phi) \times \cos\theta \sin\theta \, d\theta d\phi. \tag{13}$$

The advantage of including the factor $1/\pi$ in the expression for the emerging intensity given above is that the bidirectional reflectance function equals unity when the reflected intensity is isotropic such that $\rho(\alpha, \zeta; \theta_0, \theta, \phi) = \rho(\alpha, \zeta; \theta_0)$, independent of θ and ϕ. This assumption, known as Lambert's law, is frequently made in radiation budget studies of the earth's atmosphere and will be made for the results presented in Section 4a. Results for non-Lambertian reflectances will be presented in Section 4b.

By using Eqs. (7), (9) and (12), F_{meas} can be shown to yield

$$F_{\text{meas}} = \pi^{-1}\int_0^{2\pi}\int_0^{\alpha_m} F^+(\alpha, \zeta; \theta_0)\rho(\alpha, \zeta; \theta_0, \theta, \phi) \times \chi(\alpha,\epsilon) \sin\alpha \, d\alpha d\zeta. \tag{14}$$

The angles θ and ϕ which appear in the bidirectional reflectance function can be related to the angles α and ζ through appropriate coordinate transformations. Thus it can be shown that

$$\sin\theta = \frac{\epsilon \sin\alpha}{(1 + \epsilon^2 - 2\epsilon \cos\alpha)^{1/2}}, \tag{15}$$

$$\cos\phi = \frac{\cos\theta_0 \cos\alpha - \cos\Theta_0}{\sin\theta_0 \sin\alpha}, \tag{16}$$

where the ζ dependence is implied through the solar zenith angle θ_0 defined by (1).

Even if every position of the earth-atmosphere system within the radiometer's field of view reflects radiation according to Lambert's law, the differences between Eqs. (4) and (14) are quite significant if the scene has a nonuniform, or spatially dependent, albedo. This difference, due to the strong α dependence of $\chi(\alpha,\epsilon)$, may readily be understood. Consider the atmosphere within the field of view of a satellite sensor to consist of a large number N of equal area elements, the ith one of which has a plane albedo $a(\alpha, \zeta; \theta_0) = a_i$. If the elements with the largest albedos are located near the subsatellite point, they contribute much more to the measured flux density than if they are located near the edge of the instantaneous field of view of the radiometer (see Fig. 2). The true flux density, however, is very similar for these two extreme situations since (4) does not contain any factor analogous to $\chi(\alpha,\epsilon)$. In general, the high-albedo areas, such as clouds, will be spatially distributed more evenly within the radiometer's field of view such that the most probable value for the measured flux density will lie somewhere between these two extremes.

Fig. 3 illustrates the grid system used in the present investigation to assess the magnitude of this effect. In this study it is desirable to use a grid system such that each area element has exactly the same area and such that the outermost annulus extends to α_m. This may be accomplished by subdividing the entire field of view into n_a annuli and letting each annulus contain $2j - 1$ elements, where $j = 1, 2, \ldots, n_a$ (see Fig. 3). In this way the total number of elements N is given by

$$N = \sum_{j=1}^{n_a} (2j - 1) = n_a^2. \tag{17}$$

With this choice of a grid system, the difference in earth central angle between successive annuli, given by $\alpha_{j+1} - \alpha_j$, is approximately constant. Specifically, one can show that

$$\cos\alpha_2 = (n_a^2 - 1 + \cos\alpha_m)/n_a^2, \tag{18}$$

$$\cos\alpha_{j+1} = \cos\alpha_j - (2j + 1)(1 - \cos\alpha_2), \quad j = 2, 3, \ldots, n_a, \tag{19}$$

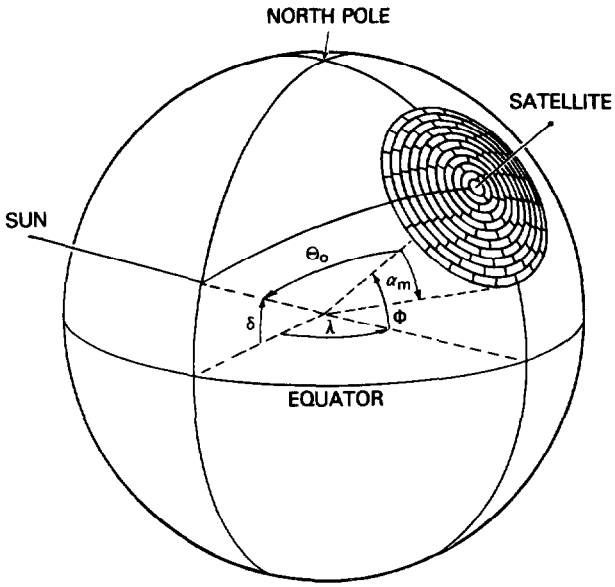

FIG. 3. Schematic illustration of the coordinate system used to simulate the variability of the reflecting atmosphere within the field of view of a satellite sensor.

where $\alpha_1 = 0°$, corresponding to the center of the spherical cap ($j = 1$), and α_{j+1} is the earth central angle corresponding to the outer limit of the jth annulus. The azimuth location of the first element in each annulus can obviously be arbitrary. Since each annulus contains an odd number of elements of equal area, we have chosen the azimuthal position of the elements such that they are symmetrically placed about the plane containing the satellite, the center of the earth and the sun, as illustrated in Fig. 3. This figure corresponds to the case of the wide field of view (WFOV) radiometer on the 600 km altitude satellite, where the height of the satellite has been exaggerated for clarity. In this case $\alpha_m = 23.33°$, $n_a = 11$ and $N = 121$.

By using (1) and (3), the measured flux density [Eq. (14)] and true flux density [Eq. (4)] can be written as

$$F_{\text{meas}} = \frac{F_0}{\pi}(\cos\Theta_0 \sum_i A_i a_i \rho_i + \sin\Theta_0 \sum_i B_i a_i \rho_i), \quad (20)$$

$$F_{\text{true}} = \frac{F_0}{2\pi(1 - \cos\alpha_m)} \times (\cos\Theta_0 \sum_i C_i a_i + \sin\Theta_0 \sum_i D_i a_i), \quad (21)$$

where

$$A_i = \int_{\zeta_i}^{\zeta_{i+1}} \int_{\alpha_i}^{\alpha_{i+1}} \chi(\alpha,\epsilon) \cos\alpha \sin\alpha \, d\alpha d\zeta, \quad (22)$$

$$B_i = \int_{\zeta_i}^{\zeta_{i+1}} \int_{\alpha_i}^{\alpha_{i+1}} \chi(\alpha,\epsilon) \sin^2\alpha \cos\zeta \, d\alpha d\zeta, \quad (23)$$

$$C_i = \int_{\zeta_i}^{\zeta_{i+1}} \int_{\alpha_i}^{\alpha_{i+1}} \cos\alpha \sin\alpha \, d\alpha d\zeta, \quad (24)$$

$$D_i = \int_{\zeta_i}^{\zeta_{i+1}} \int_{\alpha_i}^{\alpha_{i+1}} \sin^2\alpha \cos\zeta \, d\alpha d\zeta. \quad (25)$$

In these expressions α_i, α_{i+1}, ζ_i and ζ_{i+1} represent the range of earth central angles and azimuth angles of the ith elemental area (see Fig. 3). The summations in (20) and (21) extend over all area elements for which the solar zenith angle at the center of the elements is less than 90°, while the terms a_i and ρ_i represent the plane albedos and bidirectional reflectance functions at the center of the ith area element, respectively.

For the case of area elements which reflect radiation according to Lambert's law, $\rho_i = 1$ for all area elements and Eqs. (20) and (21) become

$$F_{\text{meas}} = \frac{F_0}{\pi}(\cos\Theta_0 \mathbf{A}^{\mathrm{T}}\mathbf{a} + \sin\Theta_0 \mathbf{B}^{\mathrm{T}}\mathbf{a}), \quad (26)$$

$$F_{\text{true}} = \frac{F_0}{2\pi(1 - \cos\alpha_m)}(\cos\Theta_0 \mathbf{C}^{\mathrm{T}}\mathbf{a} + \sin\Theta_0 \mathbf{D}^{\mathrm{T}}\mathbf{a}), \quad (27)$$

where the superscript T indicates a transposed vector, the elements of $\mathbf{a}$ are given by a_i, and the elements of $\mathbf{A}$, $\mathbf{B}$, $\mathbf{C}$ and $\mathbf{D}$ are given by (22)–(25). The vector $\mathbf{a}$ represents the albedos of the N different area elements and will be randomly selected as described in the next section. The elements of vectors $\mathbf{A}$, $\mathbf{B}$, $\mathbf{C}$ and $\mathbf{D}$ must be evaluated only once for each field of view and satellite altitude. These elements can be analytically derived and the results are given in the Appendix.

3. Method of solution

We consider the earth-atmosphere system within the field of view of a nadir looking satellite sensor to consist of a large number N of equal-area elements, each of which has either albedo $a_i = r_1$ (corresponding to cloudy regions) or albedo $a_i = r_0$ (corresponding to cloud-free regions). All possible combinations of cloud-free and cloudy elements in Fig. 3 correspond to possible values for the measured flux density F_{meas} and the true flux density F_{true}. It is convenient to represent a pair of possible outcomes ($F_{\text{meas}}, F_{\text{true}}$) as a point in a two-dimensional space. Both of these variables ($F_{\text{meas}}, F_{\text{true}}$) are positive and must lie within a limited range of this two-dimensional space, depending on such things as the solar zenith angle Θ_0, the altitude of the satellite (through the dependence on ϵ) and the field of view of the radiometer.

Fig. 4 illustrates these limits for the case where individual elements of the earth-atmosphere system are assumed to reflect radiation according to Lambert's law with either albedo $r_0 = 0.2$ or albedo $r_1 = 0.8$, under the conditions that $\Theta_0 = 0°$ and $\alpha_m = 23.33°$. This corresponds to the case of the WFOV radiometer on the 600 km satellite when the sun is positioned directly above the satellite. The region of Fig. 4 within the envelope represents the range of all possible outcomes of this experiment and is referred to as the sample space. A particular point within the sample space is physically realized by a potentially non-unique combination of cloud amount (i.e., number of elements with albedo r_1) and positioning of the clouds. Any pair of possible outcomes (F_{meas}, F_{true}) bears a relationship to the physical variables of the problem and is referred to as an event.

For the cases in which all elements of area within the field of view of the radiometer are illuminated by the sun (i.e., $\Theta_0 \leq 90° - \alpha_m$), as is the case in Fig. 4, the value of the true flux density F_{true} is primarily a function of the cloud amount while the large variability in the measured flux density F_{meas} is due both to the amount of clouds and their position within the radiometer's field of view. For a fixed value of F_{true}, the maximum value of F_{meas} occurs when the highly reflecting clouds are packed as near to the subsatellite point as possible while the minimum value of F_{meas} occurs when the clouds are nearest to the edge of the instantaneous field of view (IFOV) of the radiometer. This variability, due to the $\chi(\alpha,\epsilon)$ function illustrated in Fig. 2, is responsible for producing the relatively large size of the sample space illustrated in Fig. 4. The two points of intersection of the upper boundary and the lower boundary of the sample space in Fig. 4 correspond to the values of F_{true} and F_{meas} which occur when the entire atmosphere within the field of view of the radiometer has a uniform albedo (i.e., either all r_0 or all r_1 as indicated by the right-hand scale in this figure). The largest variability in F_{meas} clearly occurs for the central values of F_{true}, a region where about half of the elements have albedo r_0 and the other half have albedo r_1. The reason for the slight differences between the mean albedo scale and the F_{true}/F_0 scale in this figure is because the local solar zenith angle θ_0, and hence incident flux density $F_0 \cos\theta_0$, varies with location within the radiometer's field of view.

The large ambiguity in the reduction of satellite measured flux densities (F_{meas}) to a standard level (F_{true}) was first addressed by Bignell (1961), who observed that this ambiguity was associated with the location and intensity of scene inhomogeneities. Without doing a detailed simulation study as outlined below, he noted that the boundary of the sample space is large when the magnitude of inhomogeneities is large (i.e., large r_1/r_0) and when the altitude of the satellite is large compared to the standard level (i.e., large ϵ).

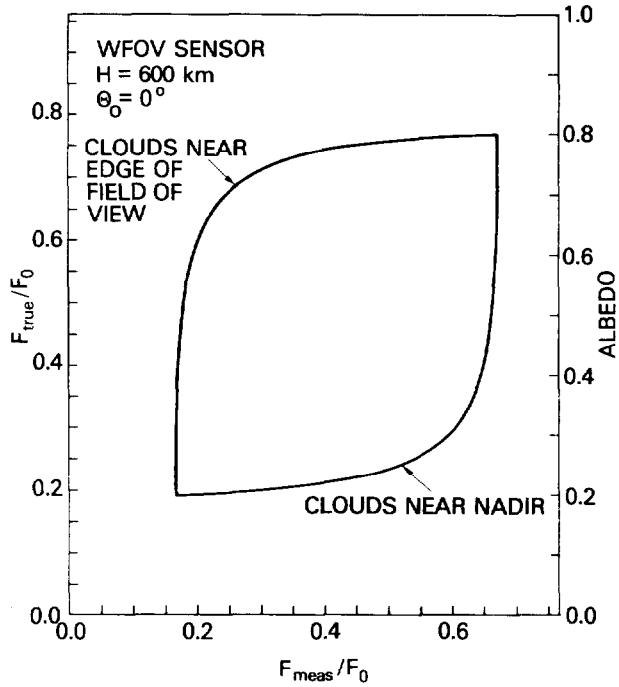

FIG. 4. Boundary of the sample space for a satellite at an altitude of 600 km which is viewing the earth-atmosphere system with a wide field of view radiometer. In this figure $\Theta_0 = 0°$ and the atmosphere is assumed to consist of elements which reflect radiation according to Lambert's law with either albedos 0.2 or 0.8.

Although an event has a relationship to the physical variables of the problem, the probability density of events within the sample space is not uniform. A joint probability density function $f(x,y)$, describing the probability that an event lies in the range x to $x + dx$ and y to $y + dy$, can be defined such that

$$1 = \int_0^\infty \int_0^\infty f(x,y)dxdy, \tag{28}$$

where $x = F_{meas}$ and $y = F_{true}$ in this problem. The probability density function $f(x,y)$, which is clearly zero outside the limits of the sample space, could be numerically derived by considering every possible combination of cloud-free and cloudy elements within the field of view of the radiometer. Denoting the number of cloudy elements by n and cloud-free elements by $N - n$, it would be necessary to compute the (F_{meas}, F_{true}) outcome for a total of

$$2^N = \sum_{n=0}^{N} \binom{N}{n} \tag{29}$$

unique combinations of cloud-free and cloudy elements, where

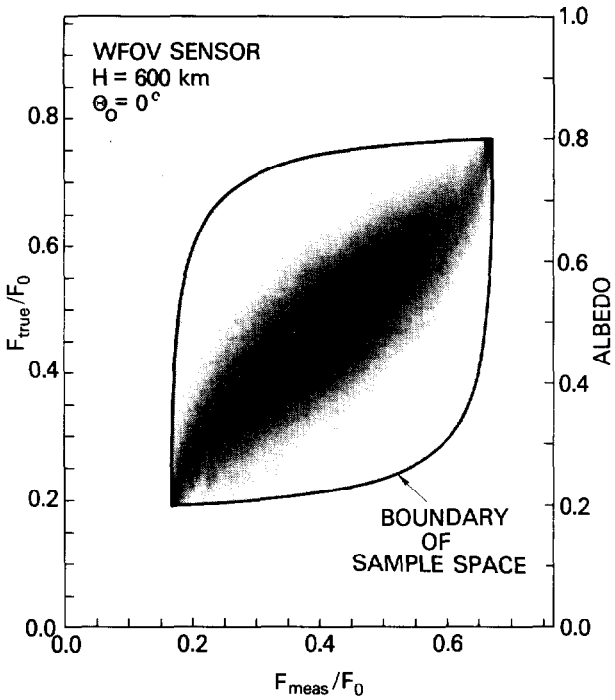

FIG. 5. Schematic illustration of the joint probability density function for the same satellite altitude and geometry presented in Fig. 4, where the gray level scale ranges between white (zero probability) and black (maximum probability).

$$\binom{N}{n} = \frac{N!}{n!(N-n)!}. \tag{30}$$

This would be a staggering task when representing the atmosphere within the field of view of the satellite sensor by a large number ($N \geq 100$) of elements, as illustrated in Fig. 3. As a consequence, it is necessary to estimate the joint probability density function with the aid of statistical sampling techniques.

If one assumes that the probability of an element being cloudy is independent of whether its neighboring elements are cloudy, the probability of observing n cloud elements and $N - n$ non-cloud elements is given by the binomial distribution as

$$P(n) = \binom{N}{n} p^n (1-p)^{N-n}, \tag{31}$$

where p represents the probability that an individual element is cloudy. In the results to be presented below it has been assumed that $p = 0.5$. The effect of this parameter will be discussed in Section 4. The sample space can be subdivided (partitioned) into $N + 1$ disjoint sets whose union is the sample space. These $N + 1$ sets represent the $N + 1$ possible causes of an experimental outcome (i.e., the $N + 1$ different number of cloud elements which could exist within the radiometer field of view). Since we are interested in obtaining the joint probability density function $f(x,y)$ that the event (x,y) occurs, the probability that the event (x,y) occurs is given by the union of the probability that each disjoint event occurs. Thus we may write

$$f(x,y) = P(0)f(x,y|0) + P(1)f(x,y|1) + \cdots$$
$$= \sum_{n=0}^{N} P(n)f(x,y|n), \tag{32}$$

where $f(x,y|n)$ represents the probability density function that the event (x,y) occurs, subject to the condition that the number of cloud elements n is certain to occur. The function $f(x,y|n)$ is referred to as a conditional probability density function (see, e.g., Hoel, 1971).

The procedure which has been adopted in the present investigation is to systematically increment the number of cloud elements n, from which it is possible to determine the binomial probability density function by using the recursion relationship

$$P(n) = \frac{N-n+1}{n} P(n-1),$$
$$n = 1, 2, \ldots, N, \tag{33}$$

where $P(0) = 2^{-N}$. For any number n of cloud elements it is possible to randomly vary the location of the cloud elements a large number M times, each time computing corresponding values of the measured and true flux densities using either (26) and (27) or the more general form (20) and (21), until an accurate estimate of the conditional probability density function $f(x,y|n)$ has been determined. Making use of (32) and (33), the joint probability density function $f(x,y)$ can thus be constructed. It is easy to show that $f(x,y)$ must obey the normalization condition (28) if $f(x,y|n)$ is similarly normalized.

For any random location of n cloud elements and $N - n$ non-cloud elements it is possible to compute not only the (F_{meas}, F_{true}) outcome associated with this situation but also the outcome associated with the inverse arrangement, that for which each cloud element with albedo r_1 is replaced by albedo r_0 and each element with r_0 is replaced by r_1. This corresponds to a particular orientation of $N - n$ cloud elements and n non-cloud elements and thus it is possible to determine $f(x, y|N-n)$ at the same time that one is determining $f(x,y|n)$. Since $P(n) = P(N-n)$ for the case where $p = 0.5$, it is possible to construct the function $f(x,y)$ by incrementing n only from 0 to $N/2$.

Fig. 5 illustrates the joint probability density function $f(x,y)$ for the same satellite altitude and geometry presented in Fig. 4. In this figure the magnitude of the probability at a particular value of F_{true} and F_{meas} is indicated by the degree of blackness, with the gray level scale ranging between white (zero

probability) and black (maximum probability). Due to the large dynamic range of $f(x,y)$ caused by the binomial probability density function $P(n)$, it was necessary in producing this figure to replace $P(n)$ by a Gaussian distribution with a larger standard deviation than $P(n)$ in order to suppress this large dynamic range. Fig. 5 thus represents $f(x,y)$ qualitatively, differing from the true density function quantitatively.

Once the joint probability density function $f(x,y)$ has been determined, it is relatively simple to compute the conditional mean value of the measured flux density, given a value of the true flux density, as well as the conditional mean value of the true flux density, given a value for the measured flux density. It is the latter conditional mean value, designed $\mu_{y|x}$, which is of interest in earth radiation budget observations since one is interested in determining the most probable value for the true flux density from a measurement at satellite altitude. It will be seen in the next section that the locus of such mean points, known as the curve of regression of $y(F_{\text{true}})$ on $x(F_{\text{meas}})$, differs substantially from a graph of the inverse problem, that of determining $\mu_{x|y}$ as a function of y. Hoel (1971) shows that the curve of regression may be determined from the joint probability density function $f(x,y)$ by

$$\mu_{y|x} = \frac{\int_0^\infty yf(x,y)dy}{\int_0^\infty f(x,y)dy}, \tag{34}$$

where the integral in the denominator of this expression is frequently referred to as the marginal density function $f(x)$. It is similarly possible to estimate the conditional variance $\sigma^2_{y|x}$ through the relationship

$$\sigma^2_{y|x} = \frac{\int_0^\infty (y - \mu_{y|x})^2 f(x,y)dy}{\int_0^\infty f(x,y)dy}. \tag{35}$$

The values of $\mu_{x|y}$ and $\sigma^2_{x|y}$ may be evaluated by expressions analogous to (34) and (35).

4. Simulation results

The method for determining the curves of regression and sample variances described in the preceding section has been used in computations simulating both wide and medium field of view radiometers carried on board satellites orbiting at both 600 and 833 km. Each of these four cases has been investigated as a function of solar zenith angle as well as for Lambertian and non-Lambertian reflectance models. A representative selection of these results is presented below.

a. Lambertian reflection

When the individual area elements of the earth-atmosphere system reflect radiation according to Lambert's law, the bidirectional reflectance function becomes unity for each area element and thus F_{meas} and F_{true} may be evaluated using (26) and (27). For consistency of presentation, all results for the Lambertian reflectances were obtained for the single situation for which the cloud-free regions have albedo $r_0 = 0.2$ and the cloud-filled regions have albedo $r_1 = 0.8$. Although these values were arbitrarily selected, the results for different values of r_0 and r_1 can easily be determined by simply scaling the results presented below. This is due to the linear dependence of F_{meas} and F_{true} on the albedo vector **a**, as seen on examination of (26) and (27).

Fig. 6a illustrates the conditional mean values of F_{meas}, given values of F_{true}, for the case of the WFOV sensor on the 600 km altitude satellite when $\Theta_0 = 0°$. This corresponds to one of the curves of regression for the joint probability density function schematically illustrated in Fig. 5, where the conditional means $\mu_{x|y}$ were determined for 60 different $y(F_{\text{true}})$ values. Since $\Theta_0 = 0°$ is a situation for which all elements within the radiometer field of view are illuminated by the sun (i.e., the terminator does not cross the IFOV), the values of F_{true} are primarily determined by the number of cloudy elements n. The variability in F_{meas}, at a given value of F_{true}, is due to the location of the clouds, with the most probable value of F_{meas} being near the center of the sample space. The error bars illustrated in Fig. 6a represent the conditional standard deviations $\sigma_{x|y}$ and thus serve to indicate the magnitude of variability to be expected in F_{meas} for any particular value of F_{true}.

In a satellite experiment the true flux density is not known but rather is to be derived from the measurements. Fig. 6b illustrates the conditional mean values of F_{true}, given values of F_{meas}, for the same satellite altitude and geometry presented in Fig. 6a. It is immediately apparent, upon examination of this figure, that the conditional means $\mu_{y|x}$ differ significantly from the conditional means $\mu_{x|y}$ presented in Fig. 6a. The curve of regression $\mu_{y|x}$ has been determined from the joint probability density function for 60 different $x(F_{\text{meas}})$ values by making use of (34). For any value of F_{meas}, it is possible that F_{true} is relatively small with the cloudy elements located near the subsatellite point as well as that F_{true} is large with the clouds located near the edge of the field of view (see Fig. 4). Since it has been assumed that the probability of there being a certain number of clouds n is given by the binomial probability density function where $p = 0.5$ [see

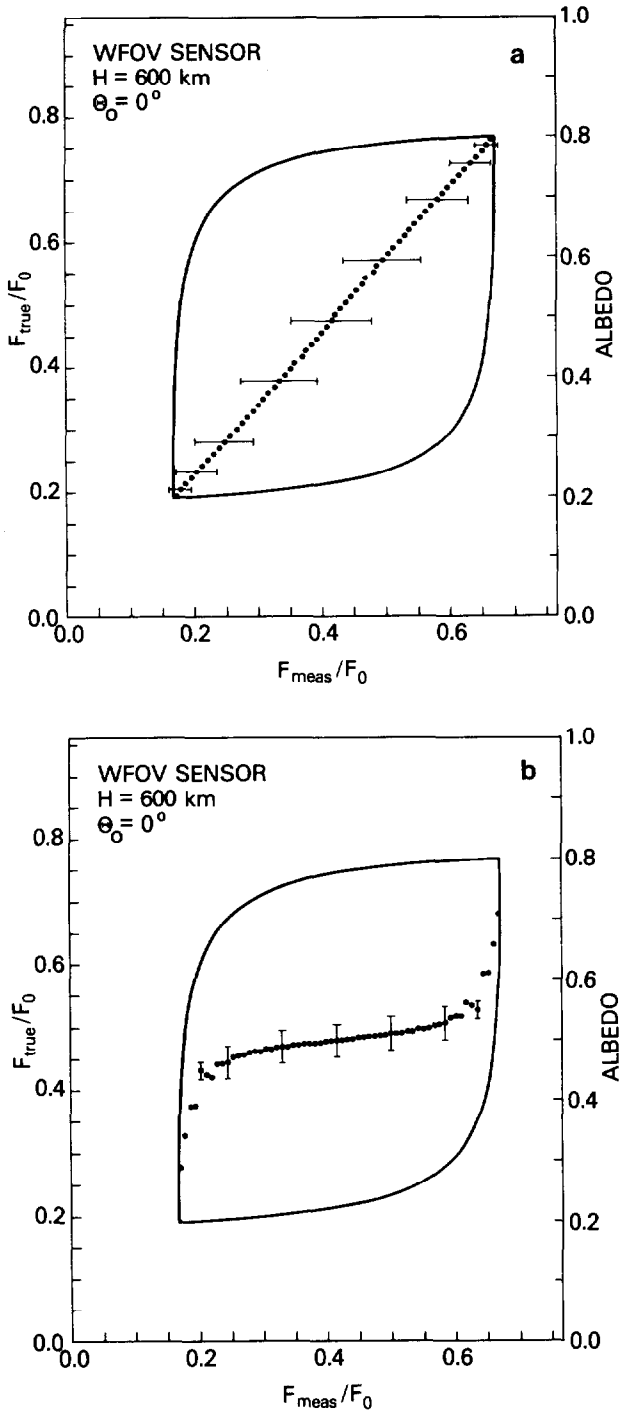

FIG. 6. The conditional means and standard deviations of (a) F_{meas}, given values of F_{true}, and (b) F_{true}, given values of F_{meas}. This case corresponds to the WFOV radiometer on the 600 km satellite when $\Theta_0 = 0°$. The limits of the sample space are also illustrated.

Eq. (31)], the most probable value of F_{true} is shifted toward the F_{true} values corresponding to 50% cloud cover. If it had been assumed that $p = 0.4$, for example, the curve of regression illustrated in Fig. 6b would be asymmetrically located within the sample space and would reflect a most probable value of F_{true} shifted toward the F_{true} values corresponding to 40% cloud cover. The curve of regression illustrated in Fig. 6a would remain essentially unaltered, being relatively insensitive to the choice of p. The effect of the curvature of $\mu_{y|x}$ can easily be deduced on examination of Fig. 5, where the magnitude of this curvature has been effectively reduced due to replacing $P(n)$ by a Gaussian distribution with the same mean value $N/2$ (i.e., pN) but with a larger standard deviation than $N^{1/2}/2$ (i.e., $[p(1-p)N]^{1/2}$. The error bars illustrated in Fig. 6b represent the conditional standard deviations $\sigma_{y|x}$ and thus serve to indicate the magnitude of variability to be expected in F_{true} for any particular value of F_{meas}. These error bars are noticeably smaller in magnitude than the values of $\sigma_{x|y}$ illustrated in Fig. 6a. This is due, in part, to the strong dependence of F_{true} on the binomial probability density function $P(n)$.

Fig. 7 illustrates the curve of regression ($\mu_{y|x}$) and standard deviation ($\sigma_{y|x}$) of F_{true} on F_{meas} for the MFOV radiometer on the 600 km altitude satellite when $\Theta_0 = 0°$. The limits of the sample space for the MFOV radiometer are noticeably more restricted in size than the corresponding limits of the sample space for the WFOV radiometer (cf. Fig. 6). The slope of the median line through the end points of the sample space $(dF_{true}/dF_{meas})_{n=N}$, designated m,

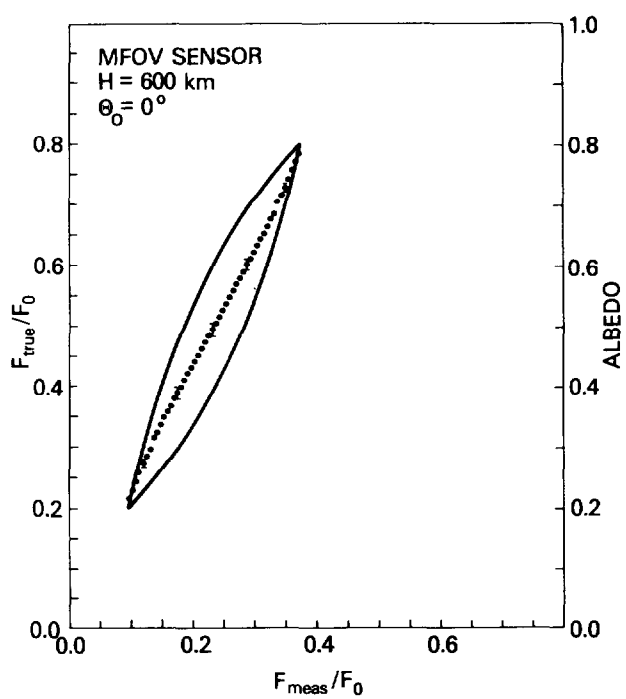

FIG. 7. The conditional means and standard deviations of F_{true}, given values of F_{meas}, for the MFOV radiometer on the 600 km satellite when $\Theta_0 = 0°$.

is also increased over the corresponding slope for the WFOV radiometer. If the sample spaces were correspondingly narrow in both of these cases, the decreased slope for the WFOV radiometer would give it a decided advantage over the MFOV radiometer in interpreting earth radiation budget observations. However, the reduction in size of the MFOV sample space leads to a less drastic effect of a variable reflectance such that there is a less dramatic shift of the curve of regression in Fig. 7 than there is in Fig. 6b. The curve of regression of F_{meas} on F_{true} ($\mu_{x|y}$) is not illustrated in Fig. 7 since it appears as a straight line passing through the end points of the sample space.

The curves of regression ($\mu_{y|x}$) and standard deviations ($\sigma_{y|x}$) of F_{true} on F_{meas} for the 833 km altitude satellite are illustrated in Figs. 8 and 9. In these figures, Fig. 8 corresponds to the WFOV radiometer while Fig. 9 corresponds to the MFOV radiometer. The solar zenith angle Θ_0 is again taken as 0° to enable ready comparison with Figs. 6 and 7. The similarities and differences between Figs. 6b and 8 and between Figs. 7 and 9 are readily apparent, with one of the major differences being the slope of the median line through the end points of the sample space.

For the cases in which all elements within the instantaneous field of view of a satellite sensor are illuminated by the sun (i.e., $\Theta_0 \leq 90° - \alpha_m$), $\sum_i B_i = \sum_i D_i = 0$, where the summations extend over all N area elements. For the case in which the earth-atmosphere system has a uniform albedo a, the measured flux density and true flux density given in (26) and (27) can be rewritten as

$$F_{meas} = \frac{F_0 a \cos\Theta_0}{\pi} \sum_i A_i, \tag{36}$$

$$F_{true} = \frac{F_0 a \cos\Theta_0}{2\pi(1 - \cos\alpha_m)} \sum_i C_i. \tag{37}$$

These values for F_{meas} and F_{true} must necessarily correspond to the end points of the sample space when $a = 0.2$ and $a = 0.8$. The value of the slope of the line which goes through these end points is thus obtained by dividing (37) by (36) and is given by

$$m = \frac{1}{2(1 - \cos\alpha_m)} \frac{\sum_i C_i}{\sum_i A_i}. \tag{38}$$

The value of the slope, given in this expression, is therefore a function of the altitude of the satellite (through A_i) and the field of view of the radiometer, but is not a function of the solar zenith angle Θ_0. The values of m for $\Theta_0 \leq 90° - \alpha_m$, together with values of α_m and ϵ, are given in Table 1 for each of the four cases considered in this investigation.

For the cases in which the terminator crosses the field of view of the radiometer, $\sum_i B_i$ and $\sum_i D_i$ are no longer equal to zero, since the summations extend only over the area elements for which the solar

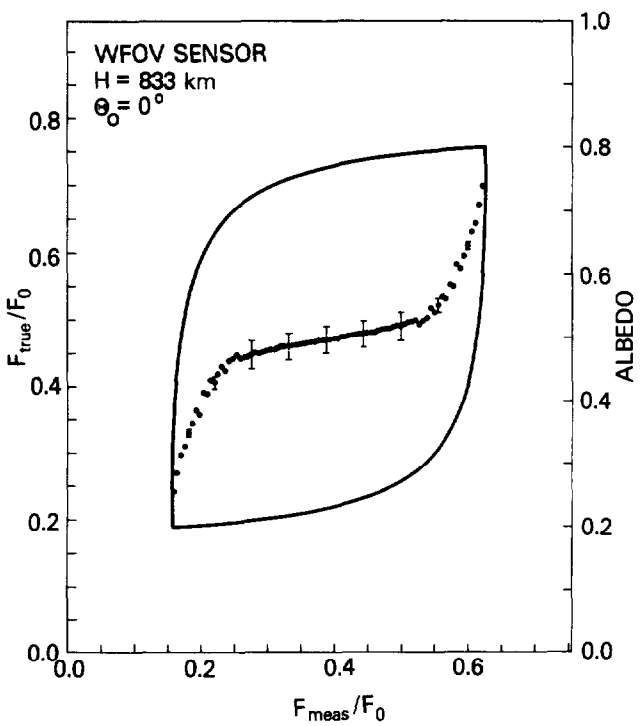

FIG. 8. As in Fig. 7 except for the WFOV radiometer on the 833 km satellite.

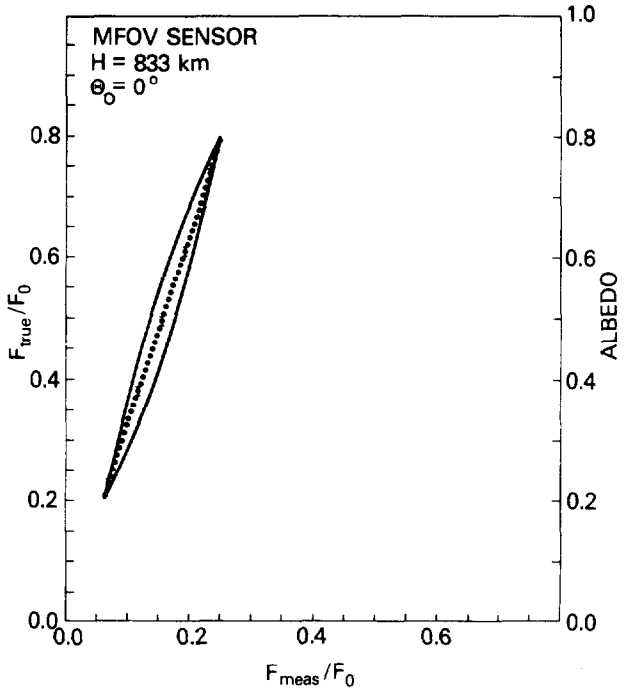

FIG. 9. As in Fig. 7 except for the MFOV radiometer on the 833 km satellite.

TABLE 1. Values of α_m, ϵ and m for the two satellite altitudes and two satellite sensors considered in this investigation.

Altitude (km)	Sensor	α_m	ϵ	m*
600	MFOV	5.00	1.0890	2.13407
600	WFOV	23.33	1.0890	1.14545
833	MFOV	5.00	1.1254	3.19849
833	WFOV	27.31	1.1254	1.20986

* The values of the slopes given here are applicable for all solar zenith angles $\Theta_0 \leq 90° - \alpha_m$.

zenith angle at the center of the elements is less than 90°. In this case the slope m is given by

$$m = \frac{1}{2(1 - \cos\alpha_m)} \times \frac{\cos\Theta_0 \sum_i C_i + \sin\Theta_0 \sum_i D_i}{\cos\Theta_0 \sum_i A_i + \sin\Theta_0 \sum_i B_i}, \quad (39)$$

and is thus a function not only of the altitude of the satellite and field of view of the radiometer but also the solar zenith angle Θ_0. The values of the reciprocal of these slopes ($1/m$) when $\Theta_0 \geq 50°$ are illustrated in Fig. 10 for all four cases considered in this investigation. It was necessary in this figure to illustrate the reciprocal of the slopes due to the fact that m approaches ∞ at large values of Θ_0 for the WFOV radiometers.

In interpreting measurements from the Earth Radiation Budget (ERB) experiment aboard the Nimbus 6 satellite, Jacobowitz *et al.* (1979) related the measured flux density to a true flux density through a simple application of the inverse square law. This is equivalent to letting $F_{\text{true}} = \epsilon^2 F_{\text{meas}}$ (i.e., $m = \epsilon^2$). As seen on examination of Table 1 for the WFOV sensors, there are systematic differences on the order of 3.5–4.5% (5.5% for the altitude of Nimbus 6, H = 1100 km) between the true flux density inferred from the inverse square law transformation and that inferred under the assumption of a uniform earth-atmosphere albedo, even when the reflected radiation is isotropic. These differences are naturally altered greatly for large solar zenith angles due to the terminator crossing the field of view of the radiometer (see Fig. 10). The inverse square law transformation, as applied by Jacobowitz *et al.* (1979), is valid strictly for a uniform reflected flux density, rather than a uniform albedo. Although the inverse square law transformation systematically *overestimates* the true flux density by 3.5–4.5% (when the scene has a uniform albedo), it *underestimates* the mean albedo by only ~1% (if one associates the true flux density with the incident solar flux density $F_0 \cos\Theta_0$ at the subsatellite point).

An alternative approach to interpreting WFOV earth radiation budget observations is to define the albedo as the ratio of the measured flux density to that which would have been measured if the earth-atmosphere system was a 100% diffuse reflector. Using (20) and (39), it follows that this definition leads to

$$a = \pi[\cos\Theta_0 \sum_i A_i + \sin\Theta_0 \sum_i B_i]^{-1} \frac{F_{\text{meas}}}{F_0}$$
$$= 2\pi(1 - \cos\alpha_m)m[\cos\Theta_0 \sum_i C_i + \sin\Theta_0 \sum_i D_i]^{-1} \frac{F_{\text{meas}}}{F_0}. \quad (40)$$

This is entirely equivalent to $F_{\text{true}} = mF_{\text{meas}}$ and thus does not lead to the same kind of biases as the inverse square law transformation providing the scene has a homogeneous albedo. The ambiguities associated with spatial inhomogeneities in the albedo of the scene are obviously not removed by any such approach.

In addition to the slope of the median line through the sample space, the size of the sample space is somewhat reduced for the higher altitude satellite. The curves of regression in Figs. 8 and 9 are logical extensions of the curves of regression in Figs. 6b and 7 and are what one should expect based on the re-

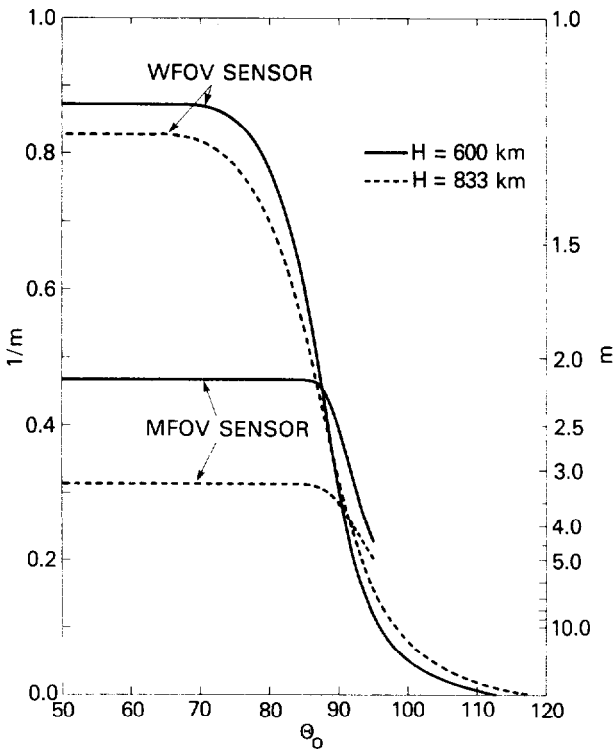

FIG. 10. Variation of $1/m$ as a function of Θ_0 showing the effects of the terminator crossing the field of view of the four satellite sensors listed in Table 1.

sults for the 600 km satellite and the differences in the sample spaces between $H = 833$ and 600 km.

When the solar zenith angle Θ_0 exceeds $90° - \alpha_m$, the curves of regression, in addition to the boundary of the sample space, begin to take on different appearances than when $\Theta_0 \leq 90° - \alpha_m$. Figs. 11a and 11b illustrate the curves of regression $\mu_{x|y}$ and $\mu_{y|x}$ for the case of the WFOV radiometer on the 600 km satellite when $\Theta_0 = 80°$. The only difference between Figs. 6a and 11a and between Figs. 6b and 11b is the solar zenith angle at the subsatellite point, with the most drastic difference being in the curve of regression ($\mu_{x|y}$) of F_{meas} on F_{true}. For a given value of the true flux density F_{true}, the most probable value of the measured flux density is systematically shifted away from the straight line of slope m which goes through the end points of the sample space. This effect only becomes evident for large values of Θ_0 and is associated with the fact that the terminator crosses the field of view of the radiometer. The curve of regression ($\mu_{y|x}$) of F_{true} on F_{meas}, which is of interest for satellite remote sensing, appears similar for all values of Θ_0 within the limits of the appropriate sample space. The fact that $\mu_{x|y}$ is not a smooth function of y in Fig. 11a is due to the fact that $f(x,y|n)$ has been estimated by randomly varying the location of the cloud elements a large number M times ($M = 12\,800$ in this case), rather than determining $f(x,y|n)$ for each possible combination of cloud-free and cloudy elements, given by (34). For the cases illustrated in Figs. 6–9, in which the terminator does not cross the radiometer's field of view, it was sufficient to let $M = 1600$.

b. Non-Lambertian reflection

In order to examine the effects of non-isotropic reflection by the earth-atmosphere system, radiative transfer calculations have been performed for cloud-free and cloudy models separately. In lieu of making time-consuming wavelength calculations, as Dave (1978) has done for four realistic cloud-free atmospheric models, we chose for this study to make computations at a single wavelength of incident illumination, given by $\lambda = 0.5550$ μm. This wavelength corresponds nearly to the peak of the incident solar spectrum and was the wavelength used in the recent theoretical sensitivity study by King and Herman (1979). The methods used to calculate the diffuse radiation field are described by Herman and Browning (1965) and Herman *et al.* (1971) for the cloud-free models and Hansen (1969) for the cloudy models. These computations were required for the solar zenith angle (θ_0), observational zenith angle (θ) and azimuth angle (ϕ) combinations of each of the illuminated area elements within the field of view of the radiometer. These angles in turn depend upon the altitude of the satellite, solar zenith angle at the subsatellite point and field of view of the radiometer, and may readily be determined through application of (1), (15) and (16). Once the albedo and bidirectional reflectance functions for each model have been determined, F_{meas} and F_{true} may be evaluated using (20) and (21).

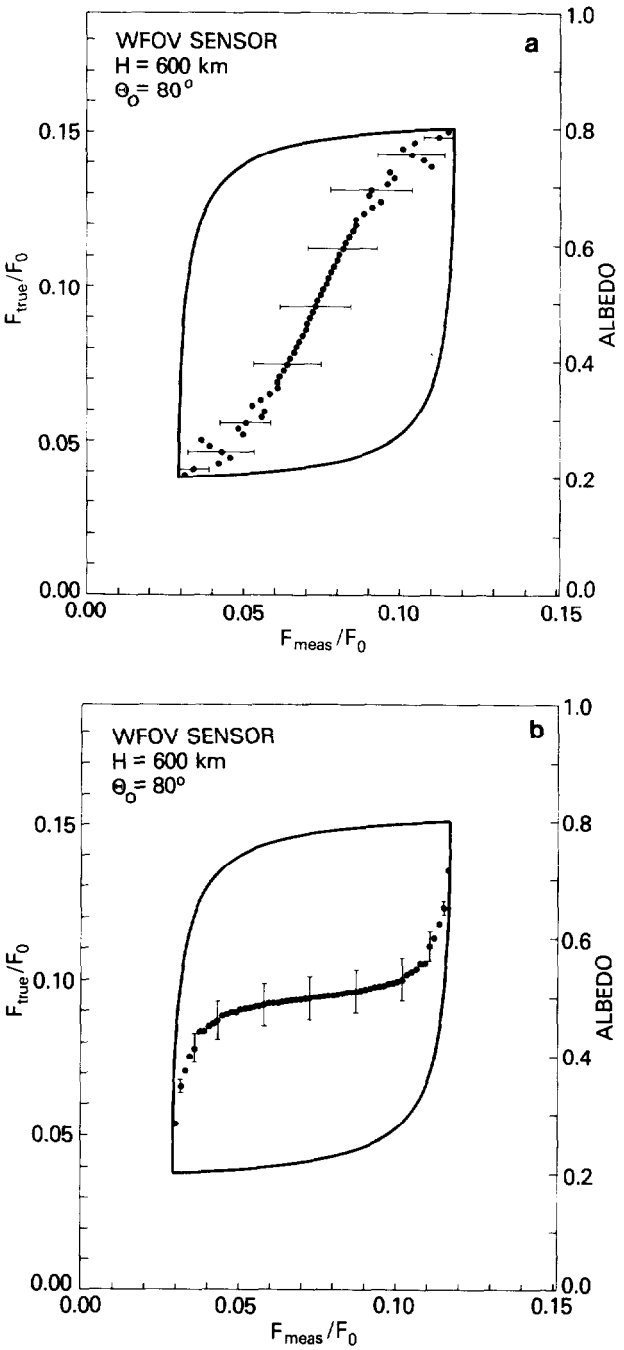

FIG. 11. The conditional means and standard deviations of (a) F_{meas}, given values of F_{true}, and (b) F_{true}, given values of F_{meas}. This case corresponds to the WFOV radiometer on the 600 km satellite when $\Theta_0 = 80°$, and is to be compared with Fig. 6.

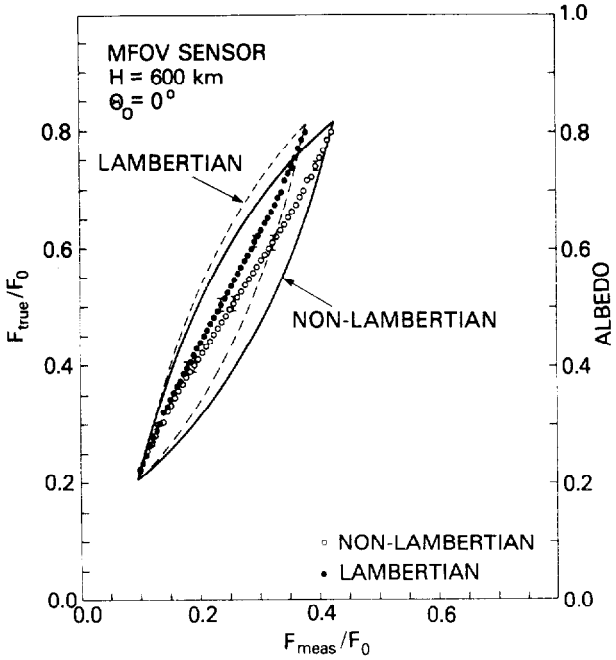

FIG. 12. The conditional means and standard deviations of F_{true}, given values of F_{meas}, for the MFOV radiometer on the 600 km satellite when $\Theta_0 = 0°$. This figure compares the results for the non-Lambertian and Lambertian reflectance models for the case where the mean albedos for the homogeneous scenes are the same.

Since F_{true} (and hence the mean albedo of the scene) depends only on the albedos of the individual area elements and not on their bidirectional reflectance functions, an attempt was made to choose the appropriate radiative transfer parameters such that the mean homogeneous cloud-free and cloudy albedos were 0.2 and 0.8, respectively. This was to enable ready comparison with the Lambertian cases presented previously (*viz.*, Figs. 6–9 and Fig. 11). For the four $\Theta_0 = 0°$ cases (two satellite altitudes and two fields of view), the geometry is such that $\phi = 180°$ for all area elements and ρ_i and a_i are only annulus dependent. For these cases the cloud-free model consisted of a vertically inhomogeneous atmosphere consisting of Rayleigh (molecular) scattering with an optical thickness $\tau_R = 0.0947$ and particulate scattering and absorption with an optical thickness $\tau_M = 0.1000$. The phase matrix of the particles is computed from Mie theory and is thus a function of the complex refractive index and size distribution of the particulates, the shape having been assumed spherical. For the computations used in this investigation, the refractive index was $m = 1.54 - 0.01i$, while the size distribution was assumed to be that proposed by Junge (1955) with $\nu^* = 3$ and the radii extending from 0.02 to 5.00 μm. Absorption by atmospheric ozone has been neglected.

In order to have an earth-atmosphere albedo of ~0.2 for this atmospheric model and for the range of solar zenith angles which occur when $\Theta_0 = 0°$, it was necessary to assume that the bottom boundary of the atmosphere reflects radiation according to Lambert's law with an albedo of 0.18. The effect of this earth-atmosphere system on the reflected intensity field, and hence on the bidirectional reflectance function, is the most significant for large zenith angles ($\theta \geqslant 60°$). Since these only occur for large values of the earth central angle α, positions for which the $\chi(\alpha,\epsilon)$ function is relatively small, the effect on the measured flux density is quite small.

The cloudy model, on the other hand, consisted of a vertically homogeneous atmosphere consisting only of scattering by cloud droplets. The refractive index of the droplets was taken as $1.33-0.00i$, while the droplet size distribution was the fair weather cumulus model defined by Hansen (1971). This distribution is a variation of the gamma distribution with a mean effective radius of 5.56 μm, where the mean effective radius differs from the simple mean radius in having the cross-sectional area of the droplets included as a weighting factor. For the wavelength and refractive index used in this investigation, this distribution is characterized by having an asymmetry factor $g = 0.8516$. The computations were obtained by using the scalar version of the doubling method [for details see Hansen (1969)] with no underlying surface albedo. In order to have an earth-atmosphere albedo of ~0.8 for this atmospheric model and for the $\Theta_0 = 0°$ cases, a cloud optical thickness $\tau_c = 52$ was selected.

Fig. 12 illustrates the conditional mean values of F_{true}, given values of F_{meas}, for the case of the MFOV sensor on the 600 km altitude satellite when $\Theta_0 = 0°$. Since the mean homogeneous cloud-free and cloudy albedos differed slightly from 0.2 and 0.8, respectively, the Lambertian model for the appropriate homogeneous albedos (*viz.*, 0.2046 and 0.8138) was run for comparison (see Fig. 12). The main differences between the Lambertian and non-Lambertian models used here are associated with the reflectance differences of the cloudy, as opposed to the cloud-free regions. Since the more realistic, non-isotropic reflectance models produce larger measurements than the corresponding isotropic (Lambertian) models, the assumption of a Lambertian atmosphere will lead to an *overestimation* of the mean earth-atmosphere albedo within the radiometer's field of view.

In addition to the case illustrated in Fig. 12, a comparison between the Lambertian and non-Lambertian models was obtained for each of the other $\Theta_0 = 0°$ cases previously illustrated (*viz.*, Figs. 6, 8 and 9). In general, the following conclusions may be drawn: 1) all essential differences between the two reflectance models were associated with the cloudy model, with little difference

associated with the cloud-free model; 2) the curves of regression were always shifted toward larger measurements in the non-Lambertian case than in the Lambertian case; 3) the line connecting the end points of the sample space does not necessarily go through the origin; and 4) the differences were insignificant in the WFOV cases and of potential importance in the MFOV cases. The most dramatic differences were for the MFOV radiometer on the 600 km altitude satellite illustrated in Fig. 12. For the small local solar zenith angles examined in these cases, and for reasonable values of the particulate optical depth in the cloud-free atmosphere, the effect of the underlying ground on the reflected intensity and bidirectional reflectance function is very important. If the ground itself has a non-Lambertian reflectance, the effects presented here would be more dependent on the cloud-free model. Koepke and Kriebel (1978) examined the influence of measured bidirectional reflectance functions of four vegetated surfaces on the radiation reflected from a realistic atmosphere. They found that differences between anisotropic and isotropic (Lambertian) ground reflection could reach as much as 10% at some observation angles when the solar zenith angle is small. Although these effects would affect the interpretation of earth radiation budget observations to some degree, they are generally small compared to the cloud effects (cf. Fig. 12).

To examine the differences between Lambertian and non-Lambertian reflectance models for large solar zenith angle cases, radiative transfer computations were again performed for cloud-free and cloudy models separately. In the case of the WFOV radiometer on the 600 km satellite when $\Theta_0 = 80°$, the terminator crosses the field of view of the radiometer. In this case the range of local solar zenith angles for which radiative transfer calculations are required is $56.7° \leq \theta_0 \leq 90.0°$. Since the albedo of the earth-atmosphere system varies significantly within this range, it is difficult to *a priori* estimate the parameters of the atmospheric models necessary to yield mean homogeneous albedos of 0.2 and 0.8. The cloud-free model selected was the same as that previously described except that the Mie (particulate) optical path was reduced to $\tau_M = 0.0500$ (i.e., $\tau_M + \tau_R = 0.1447$), while the ground albedo was reduced to 0.05. The cloud model differed only in the total optical thickness being reduced to $\tau_c = 15.5$.

Fig. 13 illustrates the conditional mean values of F_{true}, given values of F_{meas}, for this case. Since the mean homogeneous cloud-free and cloudy albedos were different than 0.2 and 0.8, the Lambertian model using the appropriate homogeneous albedos of 0.2089 and 0.7317 was run for comparison (see Fig. 13). In this case, both the cloud free *and* cloudy models contribute to a systematic increase in the satellite measurement, but these differences for the

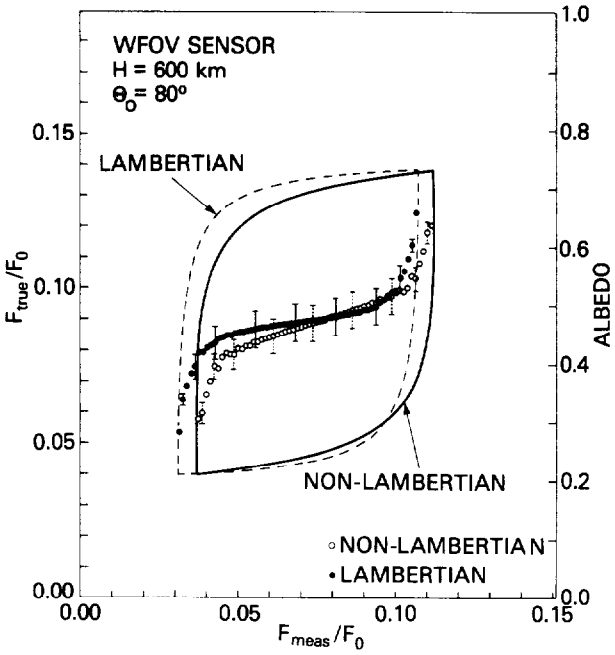

FIG. 13. As in Fig. 12 except for the WFOV radiometer on the 600 km satellite when $\Theta_0 = 80°$.

homogeneous scenes are quite small. The resulting curves of regression, on the other hand, are sufficiently different at some values of F_{meas} that an incorrect assumption of an earth-atmosphere system which reflects radiation isotropically according to Lambert's law could lead to differences in the interpretation of the mean albedo. These differences are larger for $\Theta_0 = 80°$ than for the same satellite sensor when $\Theta_0 = 0°$.

In addition to the $\Theta_0 = 80°$ case illustrated in Fig. 13, a comparison between Lambertian and non-Lambertian models was obtained for the MFOV radiometer on the 600 km satellite (see Fig. 14). The cloud-free and cloudy models were the same as in Fig. 13 but since the range of local solar zenith angles is $75° \leq \theta_0 \leq 85°$ for this case, the mean homogeneous cloud-free and cloudy albedos were again different. The Lambertian model using the appropriate homogeneous albedos of 0.2837 and 0.7876 was thus run for comparison (see Fig. 14). The differences between the Lambertian and non-Lambertian models are 1) greater for the MFOV radiometers than for the WFOV radiometers (cf. Figs. 13 and 14) and 2) these differences increase with increasing solar zenith angle (cf. Figs. 12 and 14). These difficulties with the MFOV radiometers are a result of the MFOV radiometer sampling only the reflected radiation field near the nadir observation angles, thus missing the strong forward and backward reflection lobes of the bidirectional reflectance pattern. Most of the ρ_i vector elements for both the cloud-free and cloudy models are

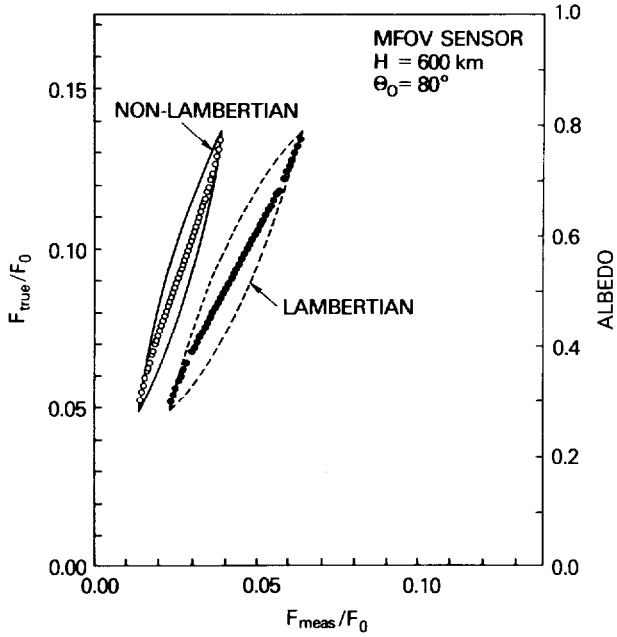

FIG. 14. As in Fig. 12 except for Θ_0 = 80°. Standard deviation estimates have not been included due to their small magnitudes.

between 0.4 and 0.6 for the Θ_0 = 80° case. The WFOV radiometer samples enough elements with high values of ρ_i to effectively eliminate this bias when the scene is homogeneous (see Fig. 13).

5. Summary and conclusions

A statistical model has been developed which aids in understanding and bounding the errors associated with the transformation of satellite measurements of the reflected flux density into flux densities leaving the top of the atmosphere. This study has concentrated on examining the differences between the measured flux density (F_{meas}) and true flux density (F_{true}) for the shortwave component of the earth radiation budget as determined from nadir viewing, fixed field of view radiometers. These differences are shown to be significant when the field of view of the radiometer is large and when the atmosphere has a nonuniform, or spatially dependent, reflectance (albedo). In addition to the effects of the field of view of the radiometer, this investigation has examined the effects of satellite altitude and solar zenith angle (including the effects of a terminator crossing the field of view of the radiometer) for both Lambertian and non-Lambertian reflectance models.

In the simulation experiment which has been described, the scene within the field of view of a nadir looking satellite sensor has been subdivided into a large number of equal-area elements, each of which reflects radiation with one of two different reflectance models (see Fig. 3). The two models which have been used represent 1) cloudy regions with high albedos and 2) cloud-free regions with much lower albedos. Figs. 6–9 and Fig. 11 illustrate the results of using the random positioning of isotropically reflecting elements, while Figs. 12–14 illustrate the compounded effects of scene inhomogeneity and the angular distribution of the reflected radiation field using realistic angular dependencies. In all instances it has been assumed that the probability of an element being cloudy is *equal* to the probability that it is cloud free (i.e., p = 0.5) and that this probability is *independent* of whether its neighboring elements are cloudy. Although the impact of the second of these assumptions is not completely known at this time, the first of these assumptions leads to the most probable value of F_{true} being shifted toward the F_{true} values corresponding to 50% cloud cover for the wide field of view radiometers (cf. Figs. 6b, 8, 11b and 13). The effect of using equal probabilities for the cloudy and cloud-free models seems to be of little importance for the medium field of view radiometers (cf. Figs. 7, 9, 12 and 14).

It is clear on examination of Figs. 7, 9, 12 and 14 that the effects of a nonuniform planetary albedo are quite small for the case of an MFOV radiometer whereas the effect of a nonuniform planetary albedo in the case of a WFOV radiometer is quite significant. Due to the large differences between the curves of regression in Figs. 6b, 8, 11b and 13 and the median line through the sample space, it is clear that large interpretation errors can arise. The fractional cloud cover, cloud-free albedos and cloudy albedos within the scene are the dominant contributors to this difference. Since these are not known *a priori*, it appears to be advantageous to make use of auxiliary information, such as that provided by a high spatial resolution scanner, in order to interpret the WFOV measurements. Additional improvement in the interpretation of WFOV observations also will arise when considering orbital simulations for which there is partial overlap in the fields of view of sequential instantaneous measurements. The effects of overlapping fields of view and repeated sampling on the spatial and temporal averages of the earth radiation budget have not been considered in the present investigation.

The effects of realistic, non-isotropic reflectance models is not of major importance for the WFOV radiometers except when the solar zenith angles are large and the terminator crosses the IFOV. Non-Lambertian effects are of great importance for the MFOV radiometers due to the smaller spatial integration of the measurements. These differences

become increasingly more important as the solar zenith angle increases.

Acknowledgments. The authors are grateful to Mr. Howard G. Meyer for invaluable assistance in computer software development and graphics and to Dr. Eric V. Slud of the Mathematics Department of the University of Maryland for valuable comments and numerous discussions concerning the statistical aspects of this research. The authors would further like to thank an anonymous referee whose careful review and comments regarding the MFOV radiometer led us to perform the computations presented in Fig. 14.

APPENDIX

The Evaluation of Vectors A, B, C and D

In order to derive analytic expressions for the elements of vectors **A** and **B**, defined by (22) and (23), it is necessary to rewrite (9) as

$$\chi(\alpha,\epsilon) = \frac{b_1 \cos^2\alpha + 2b_0 \cos\alpha + b_1}{2(b_0 + b_1 \cos\alpha)^2}, \quad \text{(A1)}$$

where

$$b_0 = 1 + \epsilon^2, \quad \text{(A2)}$$

$$b_1 = -2\epsilon. \quad \text{(A3)}$$

Substitution of (A1) into (22) leads to

$$A_i = -\tfrac{1}{2}(\zeta_{i+1} - \zeta_i) \int_{\alpha_i}^{\alpha_{i+1}} \frac{b_1 \cos^3\alpha + 2b_0 \cos^2\alpha + b_1 \cos\alpha}{(b_0 + b_1 \cos\alpha)^2} d(\cos\alpha), \quad \text{(A4)}$$

which is clearly a function only of $\cos\alpha$. By making the substitution $x = \cos\alpha$ and referring to any standard book of integral tables, it can readily be shown that

$$A_i = -\tfrac{1}{2}(\zeta_{i+1} - \zeta_i)\left[\frac{(b_0 + b_1 \cos\alpha)^2}{2b_1^3} - \frac{b_0(b_0 + b_1 \cos\alpha)}{b_1^3} - \frac{b_0(b_0^2 - b_1^2)}{b_1^3(b_0 + b_1 \cos\alpha)} - \frac{(b_0^2 - b_1^2)}{b_1^3} \ln|b_0 + b_1 \cos\alpha|\right]_{\alpha_i}^{\alpha_{i+1}}, \quad \text{(A5)}$$

which, after rearranging the order of terms, can be shown to yield

$$A_i = \tfrac{1}{2}(\zeta_{i+1} - \zeta_i)\left[\frac{b_0(b_0^2 - b_1^2)}{b_1^3(b_0 + b_1 \cos\alpha)} + \frac{(b_0^2 - b_1^2)}{b_1^3} \ln|b_0 + b_1 \cos\alpha| - \frac{\cos^2\alpha}{2b_1}\right]_{\alpha_i}^{\alpha_{i+1}}. \quad \text{(A6)}$$

The evaluation of the elements of vector **B** can be obtained as follows. Substituting (A1) into (23) leads to

$$B_i = \tfrac{1}{2}(\sin\zeta_{i+1} - \sin\zeta_i)I, \quad \text{(A7)}$$

where

$$I = \int_{\alpha_i}^{\alpha_{i+1}} \frac{b_1 \cos^2\alpha + 2b_0 \cos\alpha + b_1}{(b_0 + b_1 \cos\alpha)^2} \sin^2\alpha d\alpha. \quad \text{(A8)}$$

Due to the presence of $\sin^2\alpha$ in this expression it is not possible to obtain an integral containing only $\cos\alpha$ terms as was done in (A4). Instead it is necessary to make the substitution $x = \tan(\alpha/2)$ which, after some algebraic manipulation, leads to

$$I = 8 \int_{x_i}^{x_{i+1}} \frac{x^2[b_1(1 - x^2)^2 + 2b_0(1 - x^2)(1 + x^2) + b_1(1 + x^2)^2]}{(1 + x^2)^3[(b_0 + b_1) + (b_0 - b_1)x^2]^2} dx, \quad \text{(A9)}$$

where $x_i = \tan(\alpha_i/2)$ and $x_{i+1} = \tan(\alpha_{i+1}/2)$.

Although (A9) appears more complicated than (A8), the integrand in (A9) can be reduced by the use of partial fractions such that (A9) may be rewritten as

$$I = -\frac{8}{b_1}\int_{x_i}^{x_{i+1}} \frac{dx}{(1 + x^2)^3} + \frac{8}{b_1}\int_{x_i}^{x_{i+1}} \frac{dx}{(1 + x^2)^2} + \frac{2(b_0^2 - b_1^2)}{b_1^3}\int_{x_i}^{x_{i+1}} \frac{dx}{(1 + x^2)} - \frac{2(b_0^2 - b_1^2)(b_0 + b_1)^2}{b_1^3}\int_{x_i}^{x_{i+1}} \frac{dx}{[(b_0 + b_1) + (b_0 - b_1)x^2]^2} - \frac{2(b_0^2 - b_1^2)(b_0 - b_1)^2}{b_1^3}\int_{x_i}^{x_{i+1}} \frac{x^2 dx}{[(b_0 + b_1) + (b_0 - b_1)x^2]^2}. \quad \text{(A10)}$$

The individual integrals in this expression may readily be evaluated by making use of a table of integrals. Recalling the definition of $x = \tan(\alpha/2)$ and further noting that

$$1 + x^2 = \frac{2}{1 + \cos\alpha}, \tag{A11}$$

$$(b_0 + b_1) + (b_0 - b_1)x^2 = \frac{2(b_0 + b_1 \cos\alpha)}{1 + \cos\alpha}, \tag{A12}$$

$$\tan\frac{\alpha}{2} = \frac{\sin\alpha}{1 + \cos\alpha}, \tag{A13}$$

it can be shown that (A7) reduces to

$$B_i = (\sin\zeta_{i+1} - \sin\zeta_i)\left\{\frac{(2b_0^2 - b_1^2)}{4b_1^3}\alpha - \frac{\sin 2\alpha}{8b_1} - \frac{(b_0^2 - b_1^2)}{2b_1^2}\frac{\sin\alpha}{(b_0 + b_1\cos\alpha)} - \frac{b_0(b_0^2 - b_1^2)}{b_1^3(b_0^2 - b_1^2)^{1/2}} \times \tan^{-1}\left[\frac{(b_0 - b_1)\tan(\alpha/2)}{(b_0^2 - b_1^2)^{1/2}}\right]\right\}_{\alpha_i}^{\alpha_{i+1}}. \tag{A14}$$

The evaluation of the elements of vectors **C** and **D**, defined by (24) and (25), can readily be obtained since neither of these vectors contain the function $\chi(\alpha,\epsilon)$. Thus,

$$C_i = \tfrac{1}{2}(\zeta_{i+1} - \zeta_i)(\sin^2\alpha_{i+1} - \sin^2\alpha_i), \tag{A15}$$

$$D_i = (\sin\zeta_{i+1} - \sin\zeta_i)\left(\frac{\alpha}{2} - \frac{\sin 2\alpha}{4}\right)_{\alpha_i}^{\alpha_{i+1}}. \tag{A16}$$

REFERENCES

Bignell, K. J., 1961: Heat-balance measurements from an earth satellite—an analysis of some possibilities. *Quart. J. Roy. Meteor. Soc.*, **87**, 231–244.

Coakley, J. A., Jr., 1979: A study of climate sensitivity using a simple energy balance model. *J. Atmos. Sci.*, **36**, 260–269.

Dave, J. V., 1978: Extensive data sets of the diffuse radiation in realistic atmospheric models with aerosols and common absorbing gases. *Solar Energy*, **21**, 361–369.

Ellis, J. S., T. H. Vonder Haar, S. Levitus and A. H. Oort, 1978: The annual variation in the global heat balance of the earth. *J. Geophys. Res.*, **83**, 1958–1962.

Hansen, J. E., 1969: Radiative transfer by doubling very thin layers. *Astrophys. J.*, **155**, 565–573.

——, 1971: Multiple scattering of polarized light in planetary atmospheres. Part II: Sunlight reflected by terrestrial water clouds. *J. Atmos. Sci.*, **28**, 1400–1426.

Herman, B. M., and S. R. Browning, 1965: A numerical solution to the equation of radiative transfer. *J. Atmos. Sci.*, **22**, 559–566.

——, —— and R. J. Curran, 1971: The effect of atmospheric aerosols on scattered sunlight. *J. Atmos. Sci.*, **28**, 419–428.

Hoel, P. G., 1971: *Introduction to Mathematical Statistics*. Wiley, 409 pp.

Jacobowitz, H., W. L. Smith, H. B. Howell, F. W. Nagle and J. R. Hickey, 1979: The first 18 months of planetary radiation budget measurements from the Nimbus 6 ERB experiment. *J. Atmos. Sci.*, **36**, 501–507.

Junge, C. E., 1955: The size distribution and aging of natural aerosols as determined from electrical and optical data on the atmosphere. *J. Meteor.*, **12**, 13–25.

King, M. D., and B. M. Herman, 1979: Determination of the ground albedo and the index of absorption of atmospheric particulates by remote sensing. Part I: Theory. *J. Atmos. Sci.*, **36**, 163–173.

Koepke, P., and K. T. Kriebel, 1978: Influence of measured reflection properties of vegetated surfaces on atmospheric radiance and its polarization. *Appl. Opt.*, **17**, 260–264.

Lian, M. S., and R. D. Cess, 1977: Energy balance climate models: A reappraisal of ice-albedo feedback. *J. Atmos. Sci.*, **34**, 1058–1062.

North, G. R., and J. A. Coakley, Jr., 1979: Differences between seasonal and mean annual energy balance model calculations of climate sensitivity. *J. Atmos. Sci.*, **36**, 1189–1204.

Oort, A. H., and T. H. Vonder Haar, 1976: On the observed annual cycle in the ocean atmosphere heat balance over the northern hemisphere. *J. Phys. Oceanogr.*, **6**, 781–800.

Raschke, E., T. H. Vonder Haar, W. R. Bandeen and M. Pasternak, 1973: The annual radiation balance of the earth-atmosphere system during 1969–1970 from Nimbus 3 measurements. *J. Atmos. Sci.*, **30**, 341–364.

Vonder Haar, T. H., and V. E. Suomi, 1971: Measurements of the earth's radiation budget from satellites during a five-year period. Part I: Extended time and space means. *J. Atmos. Sci.*, **28**, 305–314.